The Astrophysical Journal, 586:344–355, 2003 March 20

PHYSICAL CONDITIONS IN THE PROTO–PLANETARY NEBULA CRL 618 DERIVED FROM OBSERVATIONS OF VIBRATIONALLY EXCITED HC_3N

F. Wyrowski,[1,2] P. Schilke,[2] S. Thorwirth,[3] K. M. Menten,[2] and G. Winnewisser[3]

Received 2002 August 14; accepted 2002 November 27

ABSTRACT

We used the Effelsberg 100 m and IRAM 30 m telescopes to observe vibrationally excited cyanoacetylene (HC_3N) in several rotational transitions toward the proto–planetary nebula CRL 618. Lines from nine different vibrationally excited states, with energies ranging up to 1600 K above ground, were detected. The lines show P Cygni profiles indicating that the HC_3N emission originates from an expanding and accelerating molecular envelope. The HC_3N rotational temperature varies with velocity, peaks at 520 K, 3 km s^{-1} blueshifted from the systemic velocity, and decreases with higher blueshift of the gas. The column density of the absorbing HC_3N is $(3–6) \times 10^{17}$ cm^{-2}. We modeled spectra based on spherical models of the expanding envelope that provided an excellent fit to the observations and discuss the implications of the models. Additionally, lines from ^{13}C substituted cyanoacetylene were observed. They can be used to constrain the $^{12}C/^{13}C$ ratio in this source to 10 ± 2.

Subject headings: circumstellar matter — line: profiles — radio lines: stars — stars: AGB and post-AGB — stars: individual (CRL 618) — stars: mass loss

1. INTRODUCTION

At the end of their lives, stars go through a sequence of red giant phases accompanied by intense stellar mass loss. This results in atomic and molecular circumstellar envelopes enshrouding the central asymptotic giant branch (AGB) stars and leading to bright infrared sources. Eventually, the star evolves into a white dwarf hot enough to ionize the envelope, starting the formation of a planetary nebula (PN). The transition phase between the AGB and PN stages is very short; consequently, objects evolving through it, so-called proto–planetary nebulae (PPNe), are very rare. Their physical and chemical properties define the starting conditions for planetary nebula evolution. Therefore, it is of importance to determine these characteristics observationally. Reviews on this subject are given in Kwok (1993) and Hrivnak (1997).

CRL 618 is the archetypical PPN. Its circumstellar, expanding envelope emits in a multitude of molecular lines (Bujarrabal et al. 1988) and contains molecules as complex as benzene, which was recently discovered with the *Infrared Space Observatory* (*ISO*) by Cernicharo et al. (2001): it shows a bipolar morphology/outflow in the optical CO and HCN emission (Meixner et al. 1998; Neri et al. 1992). The bipolar outflow lobes were imaged at high angular resolution with the *Hubble Space Telescope* (Trammell 2000). A compact, possibly variable H II region is emerging around the central star (Kwok & Bignell 1984; Martin-Pintado, Bujarrabal, & Bachiller 1993).

To study the physical and chemical properties of the circumstellar envelope of CRL 618, we started a project to observe the carbon chain molecules HCN, HC_3N, and HC_5N in their vibrationally grounded and excited states. Carbon chain molecules were chosen since they might be related to the formation of carbon dust grains. Another objective was that they provide many rotational lines of different vibrational excitation in a relatively small spectral range, allowing observations of various lines with equal spatial resolution. The vibrationally excited levels are populated by IR radiation and thus provide the interesting information about the IR fields and excitation of the gas (Wyrowski, Schilke, & Walmsley 1999) that would not be accessible in the infrared itself due to the high dust extinction.

In this paper, we present an observational study of vibrationally excited HC_3N in CRL 618 carried out using the Effelsberg 100 m and the IRAM 30 m telescopes. In the next section, we briefly describe the observing techniques. In § 3, we summarize our main results, and in § 4, the data will be interpreted in terms of an expanding, molecular circumstellar envelope. A discussion of the HC_3N analysis comparing our new results with complementary molecular studies from the literature is then given in § 5.

2. OBSERVATIONS

2.1. *Effelsberg* 100 m *Telescope*

We observed CRL 618 with the Effelsberg 100 m telescope of the Max-Planck Institute for Radioastronomy on 1998 April 23. The front end was the facility 7 mm HEMT receiver tuned to the frequency of the HC_3N $v = 0$, $J = 5–4$ transition at 45490.313 MHz. Our spectrometer was a 8192 channel autocorrelator that we used with eight overlapping subunits of 80 MHz bandwidth to cover a total of 520 MHz. The resulting spectral resolution was 0.3 MHz after smoothing the data to increase the signal-to-noise ratio. The beam at the frequencies of the HC_3N lines was 20″. Pointing was checked at roughly hourly intervals by means of continuum scans on CRL 618 itself. We found the pointing to be accurate to within 4″. Our absolute calibration was based upon continuum scans through W3(OH), 3C 84, and 3C 273,

[1] Department of Astronomy, University of Maryland, College Park, MD 20742-2421.
[2] Max Planck Institut für Radioastronomie, Auf dem Hügel 69, D-53121 Bonn, Germany.
[3] I. Physikalisches Institut der Universität zu Köln, Zülpicherstraße 77, D-50937 Cologne, Germany.

assuming flux densities of 3.5, 6, and 25 Jy, respectively, and should be accurate to 25%.

2.2. *IRAM* 30 m *Telescope*

The observations with the IRAM 30 m telescope were conducted on 1998 July 17 and 18, using the facility SIS receivers simultaneously at 109.3, 136.6, and 209.4 GHz with half-power beamwidths of 22″, 17.″6, and 11.″5 and system temperatures of 200, 350, and 500 K, respectively. Our spectrometers were an autocorrelator with 1633 channels and 0.31 MHz resolution and two filter banks with 1 MHz resolution and 512 channels. All lines were observed in the lower sideband with typical sideband rejections of 0.003, 0.025, and 0.04 at 109.3, 136.6, and 209.4 GHz, respectively. The wobbling secondary mirror was used with a beam throw of 200″ and a frequency of 0.25 MHz, resulting in spectra with flat baselines. The antenna main beam efficiencies, measured on Mars, were 0.63, 0.51, and 0.45 at 109.3, 136.6, and 209.4 GHz, respectively. We estimate that our absolute calibration uncertainy is lower than 25%.

3. RESULTS

3.1. *The* 100 m *Observations near* 45 GHz

The integrated, baseline subtracted HC_3N $J = 5$–4 spectrum of CRL 618, merging the different correlator subunits into one spectrum, is shown in the upper panel of Figure 1. The vibrational ground state line of cyanoacetylene shows a P Cygni profile, indicating that the line originates from a hot, expanding circumstellar envelope close to the exciting star. This situation is illustrated in Figure 2. In all the vibrationally excited lines, the emission part is too weak to be detected and only absorption is seen. We have detected pure rotational transitions within all fundamental bending modes ν_7, ν_6, and ν_5, the $\nu_6\nu_7$ combination mode, and the $2\nu_7$ and $3\nu_7$ overtones. The line parameters from Gaussian fits to the lines are given in Table 1. The emission and absorption features of lines showing P Cygni profiles were fitted separately. The brightness of emission lines is given in main-beam brightness temperature $T_{\rm MB}$. We report the strength of absorption features in $T_{\rm MB}/T_C$, with T_C as the continuum temperature, which is proportional to the optical depth of the lines for $T_{\rm MB}/T_C$ much smaller than unity. Another advantage of the $T_{\rm MB}/T_C$ scale is its independence from the telescope beam size since the size of the continuum source is considerably smaller then the beam (0.″1 × 0.″4; Martin-Pintado et al. 1993), as are the millimeter observations described in the next section.

3.2. *The IRAM* 30 m *Observations*

The lower three panels of Figure 1 show the spectra of HC_3N $J = 12$–11, $J = 15$–14, and $J = 23$–22. At the frequencies of $J = 12$–11 and $J = 15$–14, even more lines lines show P Cygni profiles. Comparison of all the $v_5 = 1f$ lines demonstrates the continuous transition from absorption to emission of the lines at higher frequencies. Vibrational satellites corresponding to six different modes of vibration of HC_3N can be identified. Besides the ground vibrational state, all fundamental bending modes ν_7, ν_6, and ν_5 are detected, as in the case of $J = 5$–4. In addition, the stretching vibration ν_4 and the combination mode $\nu_7\nu_4$ were detected. At 1.3 mm ($J = 23$–22), also the $2\nu_6$ overtone is detected. The latter three vibrational modes correspond to energies from 1300 to 1600 K above ground. (See vibrational energy levels in Wyrowski et al. 1999). All of the line parameters are given in Tables 2, 3, and 4. Only heavily blended lines were omitted. Several rotational lines of ^{13}C isotopomers of HC_3N in their bending modes ν_7 and $2\nu_7$ are observed as well. For all the identifications and analyses, we used the improved laboratory frequencies of Thorwirth, Müller, & Winnewisser (2000, 2001). Moreover, the 109 GHz spectrum shows the $J = 41$–40 ground state line of HC_5N along with its $v_{11} = 1e$ vibrational satellite. A study of this molecule in CRL 618 is discussed in Thorwirth (2001).

3.3. *The Continuum Emission of CRL 618*

With the MPIfR 100 m telescope, we observed drift scans centered on CRL 618 to obtain its continuum flux density. With the 30 m telescope, we estimated millimeter-wavelength continuum flux densities of CRL 618 from the total power offsets of the measured spectra, leading to consistent results between different scans. This method is reliable since we used the chopping secondary mirror so that instrumental and atmospheric drifts are kept small. The measured flux

TABLE 1
HC_3N $J = 5$–4 Line Parameters

Isotopomer	(v_4, v_5, v_6, v_7)	ℓ	ν (MHz)	$T_{\rm MB}$ or $T_{\rm MB}/T_C$ (K)	$v_{\rm LSR}$ (km s^{-1})	Δv (km s^{-1})
HC_3N	(0, 0, 0, 0)	...	45490.314e	−0.170 (20)	−38.7 (13)	11.4 (24)
	...	...	...	0.290 (50)	−16. 6 (6)	14.1 (12)
	(0, 1, 0, 0)	1*e*	45494.714e	−0.120 (20)	−27.2 (17)	14.0 (41)
	(0, 1, 0, 0)	1*f*	45520.454e	−0.064 (14)	−28.1 (7)	6.8 (15)
	(0, 0, 1, 0)	1*e*	45564.964e	−0.130 (10)	−27.3 (3)	3.5 (9)
	(0, 0, 1, 0)	1*f*	45600.785e	−0.115 (16)	−27.1 (4)	2.7 (5)
	(0, 0, 0, 1)	1*e*	45602.171e	−0.180 (16)	−31.8 (4)	12.5 (11)
	(0, 0, 0, 1)	1*f*	45667.550e	−0.240 (40)	−30.8 (4)	10.2 (10)
	(0, 0, 1, 1)	0	45727.452e	−0.040 (20)	−27.7 (7)	6.6 (11)
	(0, 0, 1, 1)	2	45729.306e	...	...	...
	(0, 0, 0, 2)	0, 2	45779.054e	−0.080 (30)	−28.9 (2)	7.3 (3)
	(0, 0, 0, 3)	1*e*	45856.001e	−0.096 (18)	−27.5 (4)	3.7 (7)

Note.—The brightness of emission lines is given in $T_{\rm MB}$, whereas absorption features are given in $T_{\rm MB}/T_C$. Heavily blended lines are omitted.

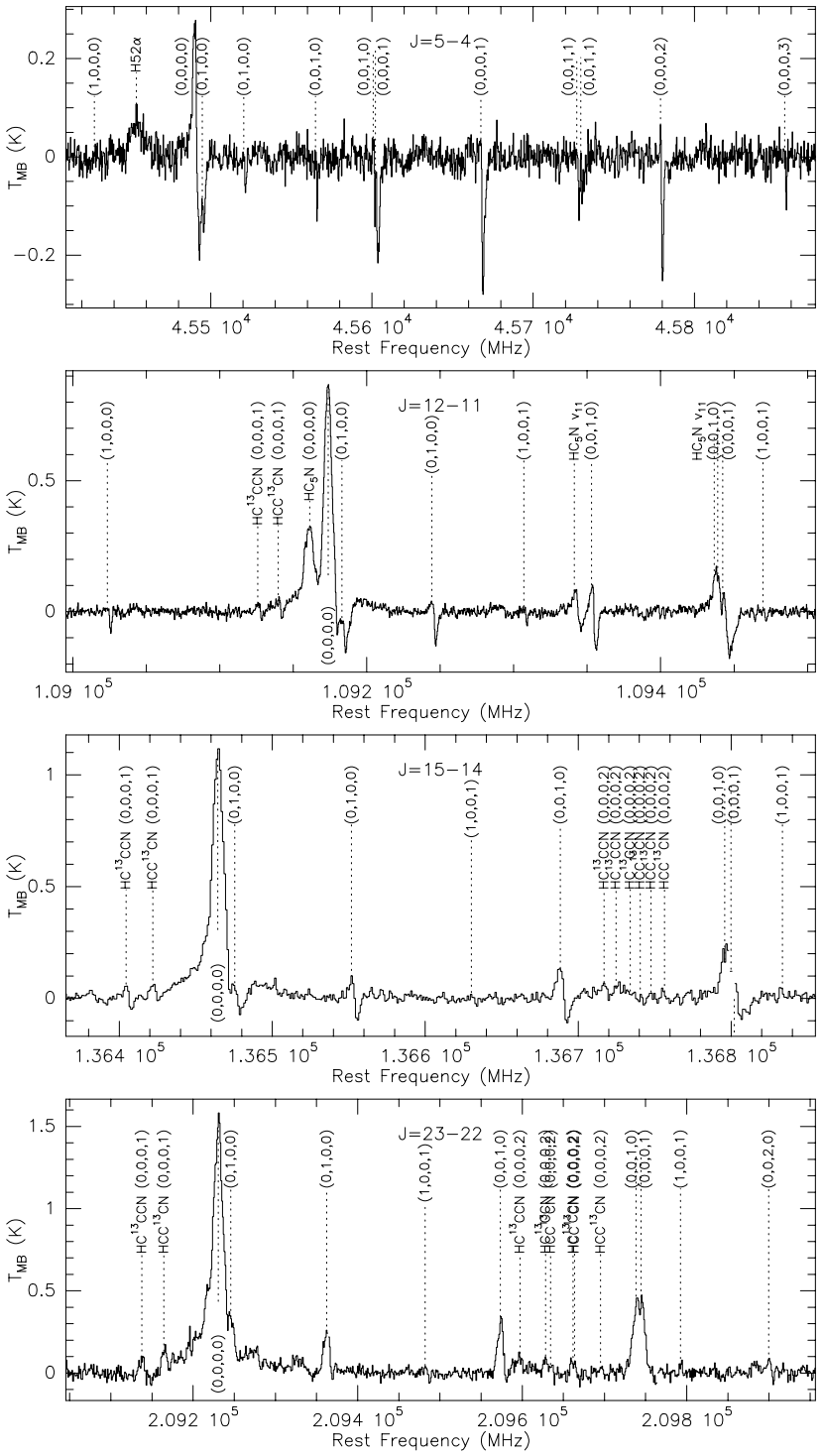

FIG. 1.—HC_3N spectra toward CRL 618

densities at all observed frequencies are given in Table 5. In addition, we use the flux densities obtained during our studies of HC_5N and HCN in CRL 618 (Thorwirth 2001; Thorwirth et al. 2002). In Figure 3, we compare the measured fluxes with continuum fluxes from the literature. At millimeter wavelengths, flux density estimates at similar frequencies agree with each other within a factor of 2, but for longer wavelengths, the spread is larger. The observations below 50 GHz were done using the VLA, the 100 m, and the Arecibo telescope. There is no trend for interferometrically determined flux densities being smaller, so we do not think the interferometer observations miss flux due to the lack of short spacings. There is also no clear trend for long-term variability: the flux measurements by Turner & Terzian (1984) at 2.4 GHz and by Knapp et al. (1995) at 8.4 GHz were performed in 1981 and 1991, respectively, and are in accordance with the recent VLA 5 GHz value by Thorwirth et al. (2002). On the other hand, variability on shorter

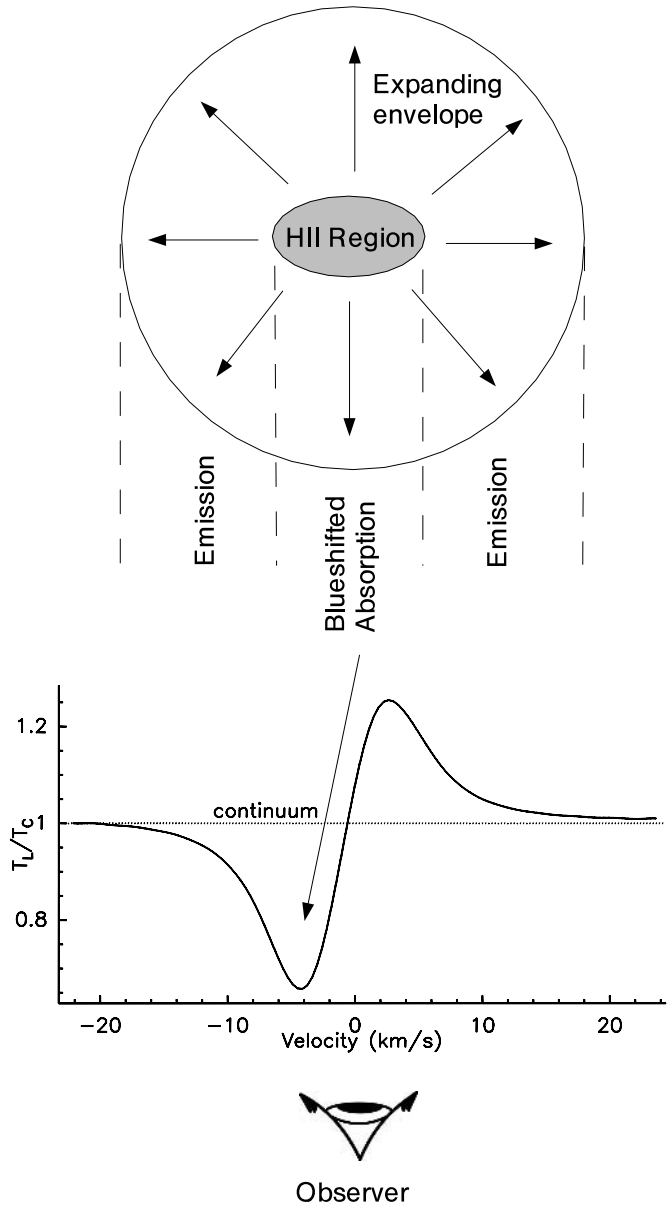

FIG. 2.—General sketch illustrating the P Cygni line profile formation in an expanding circumstellar envelope. The absorption feature is due to the blueshifted part of the envelope in front of the strong continuum from the H II region.

timescales might be the case: Kwok & Feldman (1981) reported a brightening of CRL 618 by a factor of 2 over a 2–3 yr interval at frequencies around 10 GHz. In the subsequent 5 yr, no significant increase could be detected (Martin-Pintado et al. 1988). Here we model only the continuum emission for the frequency range of 45–210 GHz covered in the present study, assuming constant flux densities in the short time interval from 1998 April–July. The fit to the continuum flux densities in Figure 3 was obtained by calculating the emerging flux from a homogeneous, circular H II region. The radius was fixed to 0.″11 (or 190 AU at a distance of 1.7 kpc; Westbrook et al. 1975) to agree with the area of the H II region obtained by Martin-Pintado et al. (1993). Then the electron temperature (T_e) and emission measure (EM) were chosen to fit the data. Our estimate for

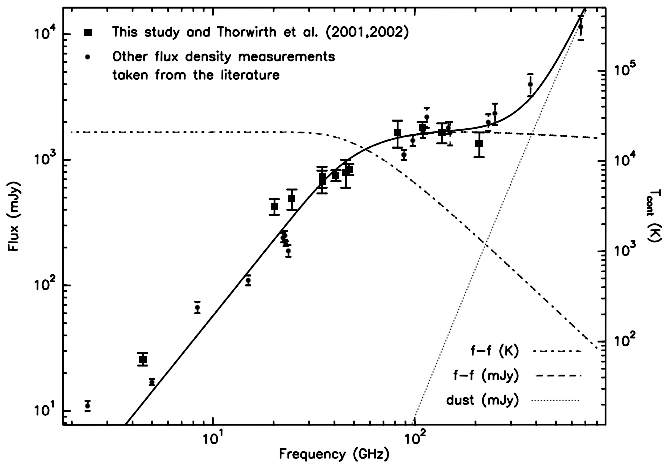

FIG. 3.—Continuum spectrum of CRL 618. *Dashed lines*: Fit of free-free emission to the flux values obtained in this study. *Dotted line*: Dust emission. *Solid line*: Sum of both components. Literature flux densities were taken from Kwok & Bignell (1984), Turner & Terzian (1984), Martin-Pintado et al. (1988), Neri et al. (1992), Knapp, Sandell, & Robson (1993), Martin-Pintado et al. (1993), Yamamura et al. (1994), Hajian, Phillips, & Terzian (1995), Martin-Pintado et al. (1995), Knapp et al. (1995), Meixner et al. (1998). In addition, the free-free emission is given in a temperature scale (see § 4.3).

EM agrees with the result by Martin-Pintado et al. (1988). The T_e from our fit is 50% higher.

4. ANALYSIS

4.1. *Velocities*

In Figure 1, the frequencies of all HC_3N lines are marked assuming a velocity of the gas of -20.5 km s^{-1}. For the emission lines, this is a good assumption, but it can be easily seen that all the absorption features are blueshifted. This situation is shown in more detail in Figure 4 for all unblended lines with mostly either emission or absorption. For the emission lines, there is little variation of velocity with upper energies of the transitions, and their average velocity is -20.6 ± 0.2 km s^{-1}. For the absorption lines, the situation is more complicated. Line velocities below 1000 K show a

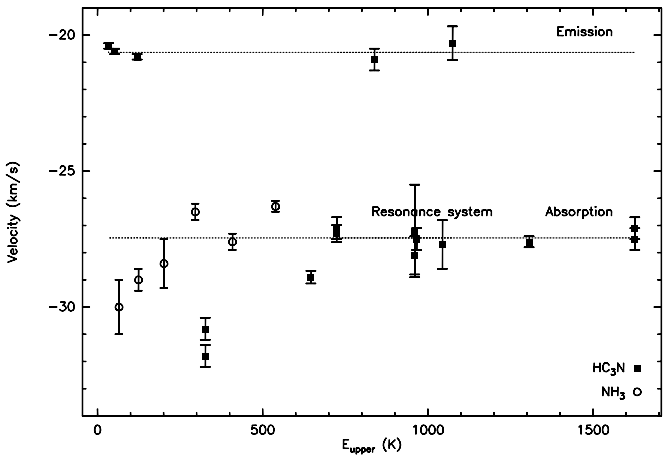

FIG. 4.—Velocities from the Gaussian fits to the HC_3N lines as a function of the upper energies of the transitions. Data from the $v_5 = 1/v_7 = 3$ Fermi resonance system are at about 1000 K.

TABLE 2

HC_3N $J = 12$–11 Line Parameters

Isotopomer	(v_4, v_5, v_6, v_7)	ℓ	Frequency (MHz)	T_{MB} or T_{MB}/T_C (K)	v_{LSR} (km s^{-1})	Δv (km s^{-1})
HC_3N	(1, 0, 0, 0)	...	109023.305	−0.220 (30)	−27.6(2)	3.7 (3)
$HC^{13}CCN$.....	(0, 0, 0, 1)	1f	109125.744e	−0.120 (30)	−28.5(4)	3.7 (9)
$HCC^{13}CN$.....	(0, 0, 0, 1)	1f	109139.707e	−0.150 (30)	−29.0(4)	6.2 (8)
HC_3N	(0, 0, 0, 0)	...	109173.634e	0.860 (20)	−20.4(1)	17.6 (1)
	$(0, 0, 0, 0)_{wng}$	...	109173.634e	0.100 (10)	−14.0(14)	124.0 (50)
	(0, 1, 0, 0)	1f	109244.222	−0.330 (50)	−28.9(2)	5.6 (4)
	...	...	...	0.040 (10)	−19.6(8)	7.9 (19)
	(1, 0, 0, 1)	1e	109306.704e	−0.150 (30)	−27.1(4)	2.7 (9)
	(0, 0, 1, 0)	1e	109352.781e	−0.420 (50)	−30.4(3)	6.0 (5)
	...	...	...	0.090 (10)	−22.2(6)	9.8 (14)
	(1, 0, 0, 1)	1f	109469.409e	−0.100 (30)	−27.5(4)	4.1 (8)

Note.—The notation $(0, 0, 0, 0)_{wng}$ acounts for the line wings of the ground state transitions originating from the high-velocity molecular outflow.

TABLE 3

HC_3N $J = 15$–14 Line Parameters

Isotopomer	(v_4, v_5, v_6, v_7)	ℓ	Frequency (MHz)	T_{MB} or T_{MB}/T_C (K)	v_{LSR} (km s^{-1})	Δv (km s^{-1})
$HC^{13}CCN$.....	(0, 0, 0, 1)	1f	136404.396e	−0.166 (21)	−28.9 (8)	4.9 (12)
	...	...	...	0.060 (10)	−19.8 (7)	5.6 (12)
$HCC^{13}CN$.....	(0, 0, 0, 1)	1f	136421.848e	−0.094 (25)	−29.7 (22)	5.6 (34)
	...	...	...	0.050 (10)	−19.7 (10)	7.2 (16)
HC_3N	(0, 0, 0, 0)	...	136464.411e	0.900 (20)	−20.6 (1)	16.5 (3)
	$(0, 0, 0, 0)_{wng}$	...	136464.411e	0.200 (20)	−21.9 (10)	97.6 (33)
	(0, 1, 0, 0)	1f	136551.798	−0.306 (39)	−29.5 (5)	5.3 (9)
	...	...	...	0.100 (10)	−20.3 (8)	5.9 (16)
	(0, 0, 1, 0)	1e	136688.252e	−0.336 (45)	−31.3 (10)	6.2 (16)
	...	...	...	0.140 (20)	−19.0 (8)	8.8 (13)

TABLE 4

HC_3N $J = 23$–22 Line Parameters

Isotopomer	(v_4, v_5, v_6, v_7)	ℓ	Frequency (MHz)	T_{MB} or T_{MB}/T_C (K)	v_{LSR} (km s^{-1})	Δv (km s^{-1})
$HC^{13}CCN$.....	(0, 0, 0, 1)	1f	209137.396	0.110 (30)	−20.6 (8)	10.1 (16)
$HCC^{13}CN$.....	(0, 0, 0, 1)	1f	209164.141	0.130 (30)	−21.6 (7)	9.1 (12)
HC_3N	(0, 0, 0, 0)	...	209230.234	1.120 (50)	−20 .8 (1)	17.6 (4)
	$(0, 0, 0, 0)_{wng}$	...	209230.234	0.370 (50)	−20.6 (10)	94.6 (33)
	(0, 1, 0, 0)	1f	209362.113	0.260 (40)	−20.3 (4)	11.3 (9)
	(0, 0, 1, 0)	1e	209573.178	0.320 (40)	−20.9 (4)	10.2 (8)
$HC^{13}CCN$.....	(0, 0, 0, 2)	0	209597.019[a]	0.040 (20)	−20 (2)	9 (2)
	(0, 0, 0, 2)	2f	209628.074[a]	...	...	...
	(0, 0, 0, 2)	2e	209661.546[a]	...	...	...
$HCC^{13}CN$.....	(0, 0, 0, 2)	0	209634.22[a]	...	...	...
	(0, 0, 0, 2)	2f	209663.206[a]	...	...	...
	(0, 0, 0, 2)	2e	209694.908[a]	...	...	...

[a] Line parameters were kept the same for all lines.

TABLE 5
OBSERVED CONTINUUM FLUX DENSITIES OF CRL 618

Frequency (GHz)	Flux (mJy)	Error (mJy)
4.5[b]	26	3
20.2[b]	425	60
24.7[b]	490	90
34.8[b]	680	140
34.8[c]	740	140
40.8[b]	750	75
45.6[a]	800	200
47.2[b]	840	85
82.3[c]	1650	400
109.2[a]	1800	200
136.5[a]	1650	300
209.0[a]	1350	340

[a] This study.
[b] Thorwirth et al. 2002.
[c] Thorwirth 2001.

rising blueshift with decreasing energies above ground. Above 1000 K, the velocities of the absorption is almost constant with a velocity of -27.2 ± 0.2 km s^{-1}. In the framework of an expanding cooling envelope, this can be interpreted as lower energy lines absorbing mainly from cooler parts of the envelope and higher energy lines from hotter parts closer to the exciting star. A constant velocity for lines higher than 1000 K means that no HC_3N is found closer to the star, hence marking the radius of the envelope where the temperature gets small enough that HC_3N is more effectively produced than destroyed.

For comparison, NH_3 line velocities taken from Martin-Pintado & Bachiller (1992) are shown in Figure 4 as well. A rising blueshift with decreasing energies can also be seen in NH_3 but shifted to lower energies above ground. In addition, Martin-Pintado & Bachiller (1992) found another absorption component at about -56 km s^{-1} that was later interpreted (Martin-Pintado et al. 1993, 1995) as being due to postshocked gas from the interaction of the high-velocity outflow with the expanding AGB envelope. In this picture, ammonia absorption is found symmetrically at ± 15 km s^{-1} from the terminal velocity of the unshocked AGB envelope at -40 km s^{-1}. This situation is illustrated in Figure 5 of Martin-Pintado et al. (1995). In contrast, the HC_3N absorption profiles are single-peaked, suggesting that HC_3N resides mainly in the unshocked gas. It follows, then, that the ammonia HC component (Martin-Pintado & Bachiller 1992) shown in Figure 4 is a blending of the redshifted lobe of the postshock material with the hot unshocked inner part of the AGB envelope seen in HC_3N.

4.2. *The High-Velocity Outflow*

The lines of the ground vibrational state of HC_3N show broad line wings. Hence, some HC_3N is found in the 200 km s^{-1} molecular outflow (Cernicharo et al. 1989; Neri et al. 1992). We fitted the line wings by masking all blending lines and the fit results are given in Tables 2–4. The lines with higher excitation do not show any detectable wings, maybe with the exception of the $J = 5$–4, $v_7 = 1f$ line. Assuming optically thin emission from the HC_3N line wings, the rotational temperature of the high-velocity gas is 60 ± 7 K where we included the HC_3N results of Cernicharo et al. (1989) into the fit. The corresponding HC_3N column density averaged over a 22″ beam is $46 \pm 9 \times 10^{12}$ cm^{-2}.

4.3. *Temperatures*

A rough estimate of the cyanoacetylene level populations can be obtained by using the lines with dominant emission features and plotting the column densities in the levels against energy above ground in a Boltzmann diagram, assuming optically thin emission. This leads to a temperature of 280 ± 20 K, which should be considered as the average over all distances from the central star. Since the optical depth of the emission lines is not known a priori, this temperature is only an upper limit.

From Figure 4, it is clear that absorption lines with velocities of -28 to -27 km s^{-1} trace the hottest component of the gas on the line of sight in front of the continuum emission. Using only these vibrationally excited lines, we estimate a temperature of 520 ± 80 K from a Boltzmann plot. Since the measured quantity $T_{\rm MB}/T_C$ is approximately $1 - \exp(\tau)$ (for $T_C \gg T_{\rm ex}$), the optical depth is known and cannot simulate a higher temperature. Figure 3 shows T_C as a function of frequency, and it is evident that for all frequencies considered in this study, $T_C > 1000$ K. The reason for the decrease in absoption with increasing frequency is that the emission gets stronger and fills up the absorption part of the line profile.

In a refinement of this method, we divided all the absorption lines into velocity bins of 2 km s^{-1} and estimated the temperature in each bin from Boltzmann plots separately. The result is shown in Figure 5 for HC_3N (5–4) and (12–11), using a systemic (stellar) velocity $v_{\rm sys}$ of -24.2 km s^{-1} (see discussion in next section). A clear increase of the temperature with lower velocities, presumably closer to the central star, is evident from the population of the vibrationally excited states in both rotational levels, confirming again the interpretation that the lines originate from an expanding cooling envelope.

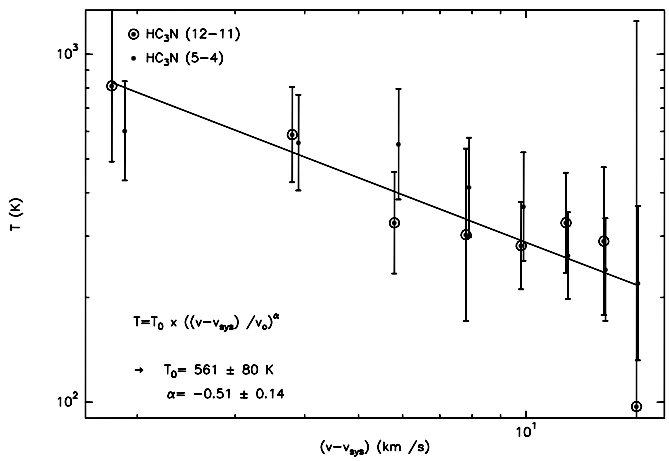

FIG. 5.—Temperature estimates from Boltzmann plots of absorption detected in different velocity bins. The temperatures have been determined for HC_3N (5–4) and (12–11) separately to test the reliability of the method. The solid shows a fit for the power-law temperature distribution discussed in § 4.4.

4.4. *A Spherical LTE Model for the Envelope*

To account for the observed P Cygni profiles, a more detailed approach is necessary. We therefore modeled an expanding spherical envelope with radial power laws for temperature, density, and velocity as follows:

$$T = T_0(r/r_0)^{\alpha_T}\ , \quad n = n_0(r/r_0)^{\alpha_n}\ , \quad v = v_0(r/r_0)^{\alpha_v}\ . \quad (1)$$

For the H II region in the center, we used the parameters derived from our continuum observations in § 3.3. We then calculated for a given molecular line and velocity the resulting intensity distribution assuming LTE conditions (see Appendix B), and from that, the emerging spectra in our observing beams. Additional free parameters are the systemic (stellar) velocity $v_{\rm sys}$ of the envelope, the intrinsic line width Δv, and the $^{12}C/^{13}C$ ratio. For the inner radius r_0, we used the radius of the H II region.

Our search for the best-fit parameters was guided by results of the previous subsections. The velocity at the inner radius $v_0 + v_{\rm sys}$ was chosen to lie close to the observed velocity of the high-energy absorption lines (Fig. 4), and the temperature at the inner radius has to be of the order of the temperature found from the Boltzmann plot of these lines. As a more quantitative approach, we fit the temperature distribution shown in Figure 5 with the power law given above and adjusted $v_{\rm sys}$ by minimizing the difference between fit and data, leading to $v_{\rm sys} = -24.2$ km s^{-1}. The resulting T_0 is close to the value estimated from the high-energy absorption lines. The resulting power-law index (β) of -0.5 constrains the ratio α_T/α_v. The ratio α_n/α_v is best determined by the total widths of the P Cygni profiles since it mainly governs out to which velocities absorption/emission is still detected. Finally, the ratio between emission and absorption peaks depends on α_v, which determines the actual spatial size of the emission; hence, a large α_v leads to small sizes and results in less emission in the modeled spectra.

At this point, it is necessary to discuss an important limitation on the accuracy of the HC_3N column density determination: the exact temperature dependence of the HC_3N partition function, including both the rotational and the vibrational part, is unknown. In a true LTE approximation, all existing energy states have to be included that, for HC_3N, due to its relatively low vibrationally excited states, leads to a sharp increase of the partition function for temperatures above about 300 K. Collisional rates for the excitation of the vibrationally excited states are mostly unknown, and the measurements and estimates that exist suggest a fast increase of the resulting critical densities with energies above ground (Wyrowski et al. 1999). On the other hand, most of the lines might be populated by infrared pumping rather than collisions. To reflect these uncertainties, we determined the column density using the two possible extreme cases: (1) counting all the states in the partition function and (2) counting only the states up to the highest observed energy above ground (see Appendix A).

For the fit, we used only unblended lines with small errors on the line frequencies. The resulting best-fit parameters are given in Table 6. The temperature exponent and the inner temperature are close to the values found by Meixner et al. (1998) for CIT 6 and CRL 618. It is clearly hotter and steeper than the temperature structure of an optically thin cloud heated by a central source ($T_0 = 420$ K, $\alpha_T = -0.4$). This is not unexpected for the dense, dusty inner part of the CRL 618 envelope. If the dust is still optically thick in the near-IR, the envelope heats itself to higher temperatures by absorbing its own thermal emission, leading to higher temperatures in the inside and a steeper temperature structure (cf. § 4.5). This power law can also be compared with results from modeling the envelope of IRC +10216, where Mamon, Glassgold, & Huggins (1998) found an inner power-law index of -0.72 by fitting the model results of Kwan & Linke (1982). Millar, Herbst, & Bettens (2000) give a temperature index of -0.79 for IRC +10216, in excellent agreement with our results toward CRL 618.

TABLE 6
BEST-FIT PARAMETERS FOR EXPANDING ENVELOPE MODEL

Description	Parameter	Value
Temperature	T_0	560 (K)
	α_T	-0.8
Density (cm^{-3})	n_0	500–1000
	α_n	-4 to -5
Velocity	$v_{\rm sys}$	-24.2 (km s^{-1})
	v_0	3.3 (km s^{-1})
	α_v	1.6
	Δv	4 (km s^{-1})
$^{12}C/^{13}C$.....	X	10
H II region	T_e	20,900 (K)
	EM	4.2×10^{10} (cm^{-6} pc)
	r_0	0.″11

NOTE.—The variation in the HC_3N density parameters reflect the uncertainty in the partition function calculation.

For a spherical wind, the equation of continuity requires a density exponent of $-(2 + \alpha_v)$. We model a steeper density exponent than this for both forms of the partition function. Since the HC_3N density is simply n_{H_2} times $X(HC_3N)$, the HC_3N abundance, this probably means that HC_3N is destroyed or converted into more complex molecules in the flow.

Fits to data are shown in Figure 6. Most lines show excellent agreement between data and model that is very surprising, given the simple assumptions used. The remaining small differences can be probably attributed to violations of the assumptions, notably local thermodynamical equilibrium and spherical symmetry. (CRL 618 does have a bipolar flow.)

4.5. *Exact Modeling of the Dusty Circumstellar Envelope*

The results of our LTE analysis of the envelope in the last section can be compared with exact modeling of the envelope using calculations of the radiative transport in dusty shells (Wolfire & Cassinelli 1986; Ivezić, Nenkova, & Elitzur 1999).[4] For the DUSTY modeling, we used a 30,000 K blackbody as radiation source, a mixture of Draine & Lee (1984) silicates and graphite with a standard MRN grain size distribution, and a dust temperature of 800 K at the inner boundary. The density structure was derived within DUSTY from full dynamics calculations. The remaining free parameters are the optical depth and the thickness of the envelope. Figure 7 shows the model results compared to measured *IRAS* and JCMT flux densities (Knapp, Sandell, & Robson 1993). The optical depth (τ_V) determines the

[4] Go to http://dustem.astro.umd.edu for DIRT and http://www.pa.uky.edu/~moshe/dusty for more information on DUSTY.

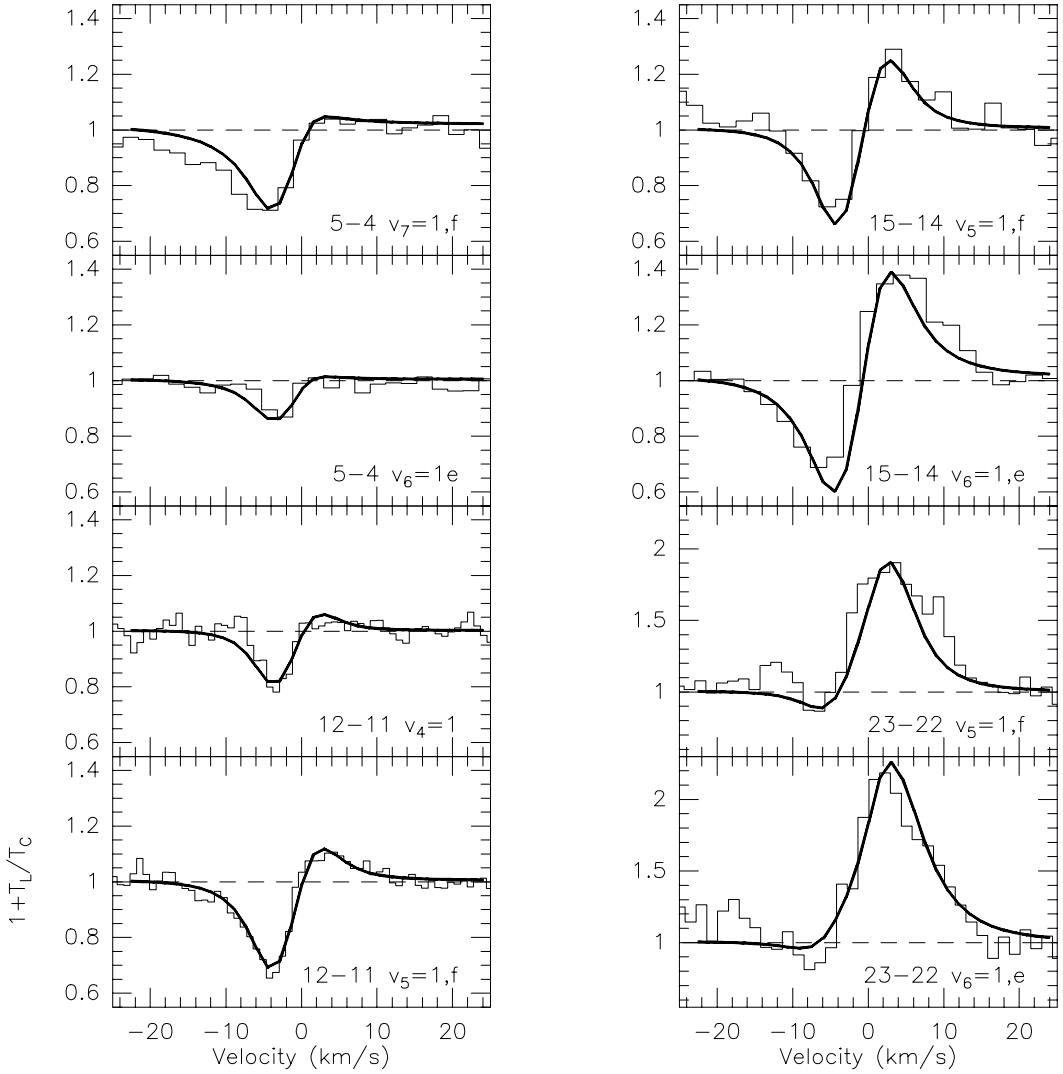

FIG. 6.—Comparison between observations (*histogram*) and line profiles from the model described in § 4.4. The velocity scale is relative to the systemic velocity.

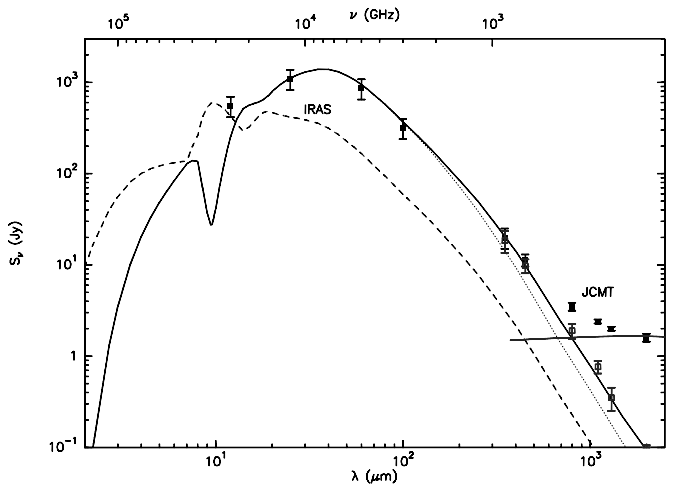

FIG. 7.—DUSTY models of the CRL 618 SED compared with *IRAS* and SCUBA data (Knapp, Sandell, & Robson 1993). *Open squares*: Corrected for free-free flux, which is shown with a separate solid line). *Solid line*: Model with $\tau_V = 100$ and thickness $s = 3000$. *Dotted line*: Same model with $s = 1000$. *Dashed line*: Model with $\tau_V = 10$.

overall shape of the SED, whereas the thickness $[s = r(\mathrm{out})/r(\mathrm{in})]$ modifies only the submillimeter part of the SED. We subtracted the free-free contribution originating from the H II region (cf. § 3.3) from the submillimeter emission. The SED shape of the DUSTY models is independent of the luminosity, which just scales the model fluxes up or down. An adequate fit to the data is reached using $\tau_V = 100$, a thickness $s = 3000$, and a luminosity of $2 \times 10^4\ L_\odot$. The radius r(in) is the dust sublimation radius that, for this model, is $0\farcs11$; hence, this is the same radius we used in the last section. The outer radius r(out) of $330''$ is comparable to the $400''$ observed by Speck, Meixner, & Knapp (2000) with *ISO*. As seen in the figure, a smaller outer radius cannot reproduce the submillimeter flux densities.

While these results are interesting in their own right, for our interpretation of the vibrationally excited HC_3N lines, only the inner part—especially the high optical depths—of the envelope is relevant. We checked the inner temperature structure (thickness $s < 10$) of DUSTY and DIRT models with high optical depth to fit the SED and found that the temperature falls off considerably faster than in the optically thin case. While the exact structures of the models differ, they

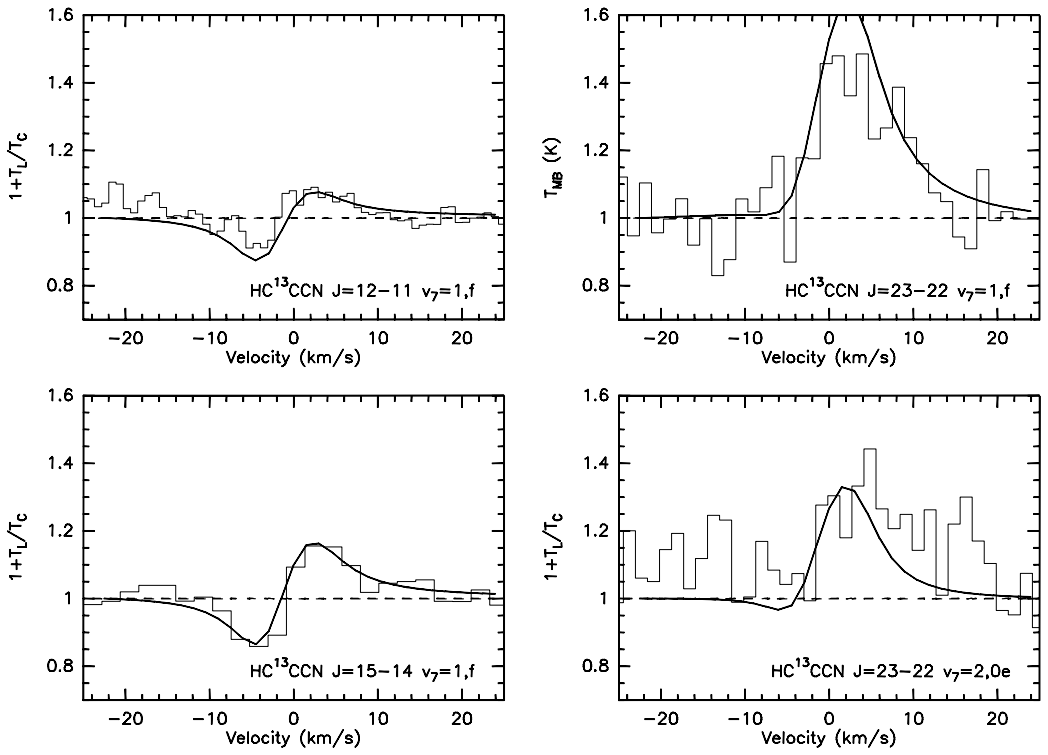

FIG. 8.—Comparison between observations (*histogram*) and line profiles from the model described in § 4.4 for lines of $HC^{13}CCN$

can be roughly approximated with $\alpha_T = -0.8$ power laws; hence, consistent with the results of the last section.

Since DUSTY allows us also to model the envelope expansion by assuming that it is driven by radiation pressure on the dust grains (Ivezić & Elitzur 1995; Elitzur & Ivezić 2001), we can compare the velocity structure predicted by DUSTY with our results from the last section. The model used to fit the SED leads to a terminal wind velocity v_∞ of 4 km s^{-1} for a gas-to-dust ratio $r_{\rm gd} = 200$ and a dust grain bulk density $\rho_s = 3$ g cm^{-3}. The terminal wind velocity (v_∞) scales with $(r_{\rm gd}\rho_s)^{-1/2}$ (see Elitzur & Ivezić 2001 for details). Hence, explaining a v_∞ of the order of 20 km s^{-1}, as implied by our data, would require very unlikely values for $r_{\rm gd}$ and/or ρ_s. But, even then, the P Cygni profiles predicted by a DUSTY velocity structure would be very broad and less peaked than the observed ones. The reason is that for radiatively driven, optically thick winds, most of the acceleration takes place in a very thin part of the shell: 90% of v_∞ is reached already at about $2r_{\rm in}$. We therefore conclude that the expansion of the CRL 618 envelope cannot be due exclusively to radiation pressure and other processes have to be invoked, e.g., processes related to the powerful outflow associated with CRL 618.

4.6. *The Total Absorbing Column Density and the* $^{12}C/^{13}C$ *Ratio*

The observed absorption lines can be used to estimate the HC_3N column density on the line of sight. As discussed in the last section, the major uncertainty here is the partition function. We again use two extreme cases to constrain the column density; at a temperature of 520 K (§ 4.3), the HC_3N column density is (3–6) $\times$ 10^{17} cm^{-2}.

To estimate the $^{12}C/^{13}C$ ratio to a high accuracy, we determined the minimum χ^2 sum between data and model for the HC_3N $v_5 = 1f$ and the $HC^{13}CCN$ $J = 15$–14, $v_7 = 1f$ lines. These lines were chosen because they appear to be unblended and were observed simultaneously with the same receiver. Hence, in the ratio, all calibration uncertainties cancel out. Appearing mostly in absorption, these 3 mm lines are much more sensitive to column density than the corresponding ^{12}C, ^{13}C lines at the higher frequencies. The errors in the resulting densities were determined by varying the densities around the best-fit values. This leads to a $^{12}C/^{13}C$ ratio of 10 ± 2 and the model fits to all of the $HC^{13}CCN$ lines are shown in Figure 8.

5. DISCUSSION AND CONCLUSIONS

Our results include the best determination of the temperature structure in CRL 618 so far. The method we used offers several advantages. (1) Highly excited absorption lines of HC_3N in vibrationally excited states are able to probe the hottest, inner part of the molecular envelope in a pencil beam. Since vibrationally excited lines with the same J_u are observed simultaneously, their relative calibration is excellent, and the peak temperature found is 520 ± 80 K. (2) Due to the expansion of the envelope, the temperature structure can be determined as a function of velocity. (3) From the emission part of the observed P Cygni spectra, the spatial extent of the envelope at a certain velocity can be determined, which then leads to temperature structure as a function of radius ($T \propto r^{-0.8}$).

How does our result compare with previous measurements? Cernicharo et al. (2001) find a temperature of 200 K from their *ISO* mid-IR observations of HCN and C_2H_2. They were not able to resolve the velocity structure and therefore probe with their absorption lines an average over the whole line of sight; hence, a lower temperature. In the analysis of far-IR *ISO* observations of CRL 618 Herpin & Cernicharo (2000) distinguish between different shells close to the central star, with temperatures of 1000, 800, and 250 K, decreasing away from the star with radii of 0.″3, 0.″5, and 0.″8, respectively. The shells with temperatures higher than our estimate seem to probe a photon-dominated region, where HC_3N might not yet exist. Exact modeling of the dusty circumstellar envelope using DUSTY was able to reproduce the temperature structure and the spectral energy disribution but failed to predict the observed velocity structure of the envelope, indicating that radiation pressure alone is not sufficient to drive the expansion.

Isotopic abundance ratios in AGB stars deliver, in principle, valuable information on nuclear processes and dredge up convective processes that bring up enriched material into the stars' outer layers, from which they finally end up in the circumstellar envelopes (Balser, McMullin, & Wilson 2002 and references therein). The HCCCN/HC^{13}CCN abundance ratio of 10 we determine is much lower than the solar system value of 89. Our ratio is very similar to the $^{12}CO/^{13}CO$ ratio of 11.6 derived by Wannier & Sahai (1987) for CRL 618, which is the lowest they found for any of the 10 C and one S stars they investigated. The $^{12}CO/^{13}CO$ ratios for the other stars in their sample range from 14 to 48. In contrast, Kahane et al. (1992) derive $^{12}CO/^{13}CO = 18$ and 3.2 for the 1–0 and 2–1 rotational lines, respectively, for CRL 618. However, they adopt a *lower limit* of 30 for $[^{12}C/^{13}C]$, which they derive from the $[^{12}C^{34}S]/[^{13}C^{32}S]$ double ratio. From carbon monoxide observations, Balser et al. (2002) determined the $^{12}C/^{13}C$ ratio for 11 planetary and proto–planetary nebulae and found values between 4 and 32, with a lower limit of 4.6 for CRL 618 being at the lower end.

There are thus a number of uncertainties in the determination of the $[^{12}C/^{13}C]$ in CRL 618. However, observations of C-bearing molecules other than carbon monoxide should be useful to get a clearer picture since they might be subjected differently to fractionation and photodissociation than the CO isotopomers, where, according to Kahane et al. (1992), these processes cancel each other.

The present study was supported by the Deutsche Forschungsgemeinschaft (DFG) via Grand SFB 494. F. W. was partly supported by the National Science Foundation under grant 96-13716.

APPENDIX A

THE HC_3N PARTITION FUNCTION

The partition function can be written as the product of its vibrational and rotational part:

$$Q = Q_v \times Q_r \, . \tag{A1}$$

In cold gas, the contribution of vibrationally excited states can be neglected, and for linear molecules, the partition function is simply $Q = Q_r = 1/3 + kT/hB$. In hotter environments, molecules are excited into vibrational states, and Q_v is given in LTE as

$$Q_v = \sum_{v_1=0}^{\infty} \cdots \sum_{v_7=0}^{\infty} \exp\left[\frac{-hc\Sigma(v_i\omega_i)}{kT}\right] \prod_{i=5}^{7}(v_i + 1) \, , \tag{A2}$$

where the sums can be evaluated analytically to yield

$$Q_v = \prod_{i=1}^{7}\left\{1 - \exp\left[\frac{(-hc\omega_i)}{kT}\right]\right\}^{-d_i} \tag{A3}$$

(Herzberg 1945). Here v_i is the vibrational quantum number and d_i denotes the degree of degeneracy of vibration i with vibrational frequency of ω_i.

For non-LTE conditions, the higher levels might not be populated for two reasons: (1) Critical densities for the higher levels are generally larger so that the density might be too small to populate the level. (2) Vibrationally excited states might be excited by IR radiation fields. Higher levels correspond to shorter wavelengths in the near-IR, where the radiation might be too weak to pump the levels. Hence, to estimate a lower limit for the partition function, we computed equation (A2) only up to the highest energy observed. The resulting lower and upper limits for the vibrational part of the partition function as a function of temperature are shown in Figure 9, together with values from laboratory measurements published in the Cologne Database for Molecular Spectroscopy.[5]

[5] Go to http://www.cdms.de/.

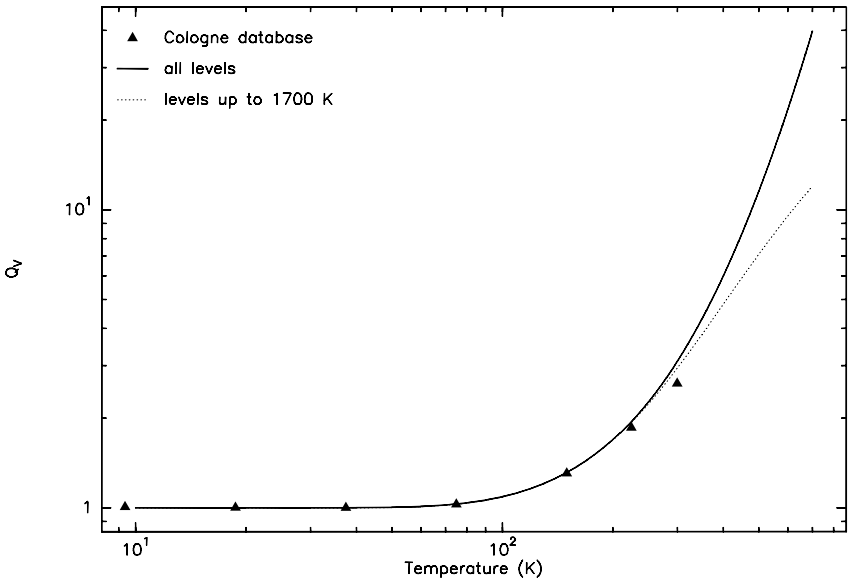

FIG. 9.—Vibrational part Q_v of the partition function as discussed in Appendix A compared with results from CDMS (Müller et al. 2001)

APPENDIX B

THE RADIATIVE TRANSFER

To calculate the intensity $I_{\rm tot}$ at a certain position R and velocity v, we integrate over the line of sight z at R as follows:

$$I_{\rm tot}(R) = \int dz(I(R,z)\ \exp[-d\tau(R,z)] + S(R,z)\{1-\exp[-d\tau(z)]\})\ . \tag{B1}$$

with

$$S(R,z) = \frac{h\nu}{\exp(h\nu/kT_{\rm ex})-1}\ . \tag{B2}$$

Here, $I(R,z)$ is the intensity integrated up to a position z on the line of sight. The variable S is the source function at a position (R,z). The variable $T_{\rm ex}$ is either the kinetic temperature T_K of the molecular gas or the electron temperature T_e of the embedded H II region. The optical depth at any position (R,z) is given as

$$d\tau(R,z) = \frac{c^2}{8\pi\nu^2}\ A\ n_u[1-\exp(h\nu/T_{\rm K})]\phi_0\ , \tag{B3}$$

with

$$\phi_0 = \frac{2c\sqrt{\log(2)}}{\nu\sqrt{\pi}\Delta v}\ \exp\left\{-4\log(2)\frac{[v-v(R,z)]^2}{\Delta v^2}\right\}\ , \tag{B4}$$

and the population of the upper states in LTE,

$$n_u = \frac{g}{Q}\ n\ \exp\left(\frac{h\nu}{kT}\right)\ . \tag{B5}$$

The optical depth through the H II region is

$$\tau_c = 0.0824\ T_e^{-1.35}\ \nu^{-2.1}\ {\rm EM}\ . \tag{B6}$$

REFERENCES

Balser, D. S., McMullin, J. P., & Wilson, T. L. 2002, ApJ, 572, 326
Bujarrabal, V., Gomez-Gonzalez, J., Bachiller, R., & Martin-Pintado, J. 1988, A&A, 204, 242
Cernicharo, J., Guelin, M., Penalver, J., Martin-Pintado, J., & Mauersberger, R. 1989, A&A, 222, L1
Cernicharo, J., Heras, A. M., Tielens, A. G. G. M., Pardo, J. R., Herpin, F., Guélin, M., & Waters, L. B. F. M. 2001, ApJ, 546, L123
Draine, B. T., & Lee, H. M. 1984, ApJ, 285, 89
Elitzur, M., & Ivezić, Z. 2001, MNRAS, 327, 403
Hajian, A. R., Phillips, J. A., & Terzian, Y. 1995, ApJ, 446, 244
Herpin, F., & Cernicharo, J. 2000, ApJ, 530, L129
Herzberg, G. 1945, Infrared and Raman Spectra of Polyatomic Molecules, Vol. 2 (New York: Krieger)
Ivezić, Z., & Elitzur, M. 1995, ApJ, 445, 415

Ivezić, Z., & Elitzur, M. 1996, MNRAS, 279, 1011
Ivezić, Z., Nenkova, M., & Elitzur, M. 1999, User Manual for DUSTY, Univ. Kentucky Rep.
Kahane, C., Cernicharo, J., Gomez-Gonzalez, J. & Guelin, M. 1992, A&A, 256, 235
Knapp, G. R., Bowers, P. F., Young, K., & Phillips, T. G. 1995, ApJ, 455, 293
Knapp, G. R., Sandell, G., & Robson, E. I. 1993, ApJS, 88, 173
Kwan, J., & Linke, R. A. 1982, ApJ, 254, 587
Kwok, S. 1993, ARA&A, 31, 63
Kwok, S., & Bignell, R. C. 1984, ApJ, 276, 544
Kwok, S., & Feldman, P. A. 1981, ApJ, 247, L67
Mamon, G. A., Glassgold, A. E., & Huggins, P. J. 1988, ApJ, 328, 797
Martin-Pintado, J., & Bachiller, R. 1992, ApJ, 391, L97
Martin-Pintado, J., Bujarrabal, V., & Bachiller, R. 1993, ApJ, 419, 725
Martin-Pintado, J., Gaume, R., Bachiller, R., Gomez-Gonzalez, J., & Planesas, P. 1988, A&A, 197, L15
Martin-Pintado, J., Guame, R. A., Johnston, K. J., & Bachiller, R. 1995, ApJ, 446, 687
Meixner, M., Campbell, M. T., Welch, W. J., & Likkel, L. 1998, ApJ, 509, 392
Millar, T. J., Herbst, E., & Bettens, R. P. A. 2000, MNRAS, 316, 195
Müller, H. S. P., Thorwirth, S., Roth, D. A., & Winnewisser, G. 2001, A&A, 370, L49
Neri, R., et al. 1992, A&A, 262, 544
Speck, A. K., Meixner, M., & Knapp, G. R. 2000, ApJ, 545, L145
Thorwirth, S. 2001, Ph.D. thesis, Univ. Cologne
Thorwirth, S., Müller, H. S. P., & Winnewisser, G. 2001, Chem. Phys., 3, 1236
———. 2000, J. Mol. Spectrosc., 204, 133
Thorwirth, S., et al. 2002, ApJL, submitted
Trammell, S. R. 2000, in ASP Conf. Ser. 199, Asymmetrical Planetary Nebulae II: From Origins to Microstructures, ed. J. Kastner, N. Soker, & S. Rappaport (San Francisco: ASP), 147
Turner, K. C., & Terzian, Y. 1984, AJ, 89, 501
Wannier, P. G., & Sahai, R. 1987, ApJ, 319, 367
Westbrook, W. E., Willner, S. P., Merrill, K. M., Schmidt, M., Becklin, E. E., Neugebauer, G., & Wynn-Williams, C. G. 1975, ApJ, 202, 407
Wolfire, M. G., & Cassinelli, J. P. 1986, ApJ, 310, 207
Wyrowski, F., Schilke, P., & Walmsley, C. M. 1999, A&A, 341, 882
Yamamura, I., Shibata, K. M., Kasuga, T., & Deguchi, S. 1994, ApJ, 427, 406